Modeling and Scale-Up of Multiwafer LPCVD Reactors

Thomas A. Badgwell, Thomas F. Edgar, and Isaac Trachtenberg
Dept. of Chemical Engineering, The University of Texas, Austin, TX 78712

The deposition of thin films in a hot-wall multiwafer low-pressure chemical vapor deposition (LPCVD) reactor is an important unit operation in the manufacture of modern integrated circuits. In this article, our previously published model for the multiwafer LPCVD reactor has been combined with in-situ temperature measurements to accurately predict the axial and radial film thickness distributions for a polysilicon deposition process. The model describes in detail multicomponent mass transport, the reactor's thermal environment based on in-situ temperature measurements, and the reactor geometry including inlet and outlet sections as well as downstream injectors. Model predictions were compared with experimental data from two industrial-scale polysilicon reactors at SEMATECH and from a smaller research reactor. Approximate scale-up rules for the important special case of larger wafers were derived from the model equations and tested by simulation. The rules compare well with the results from a nonlinear program in which the axial variation of film growth rate was minimized.

Introduction

The hot-wall multiwafer low-pressure chemical vapor deposition (LPCVD) reactor, first introduced in the late 70s (Rosler, 1977), is a critical component in the manufacture of integrated circuits. Figure 1 shows a typical configuration. Although this type of reactor is widely used to deposit polysilicon, nitride, and low-temperature oxide films (Lee, 1990; Sze, 1988), the fundamental transport phenomena and chemical reactions influencing these processes are not well understood. Industrial units are usually operated from empirical correlations that relate film characteristics to process conditions. This leads to a lack of flexibility as operating demands change and limits new reactor designs to the proven operating regions of existing systems. An accurate fundamental model would allow existing systems to be more easily optimized and would allow new reactor designs to be explored with greater confidence.

In previous work, we described a set of polysilicon deposition experiments performed both at SEMATECH and The University of Texas (U.T.), and showed how a relatively simple fundamental model can predict the basic features of the average film growth rate and radial film nonuniformity (standard de-

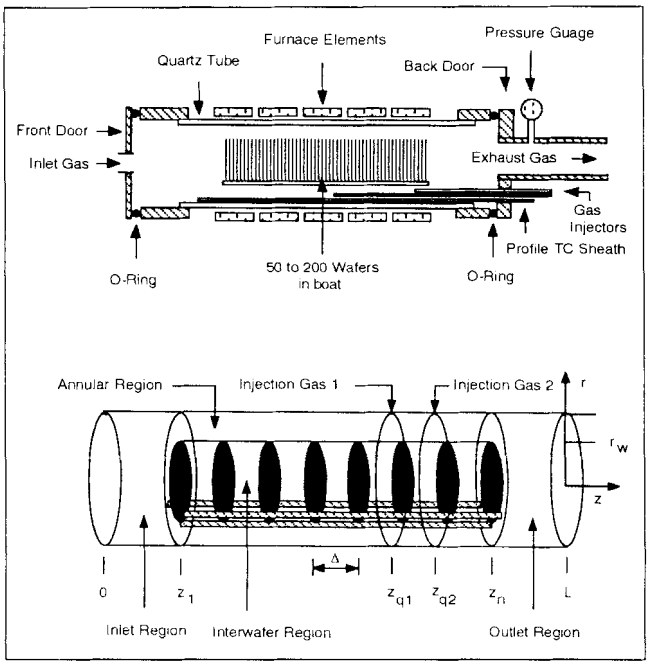

Figure 1. Typical hot-wall multiwafer LPCVD reactor and assumed model geometry.

Correspondence concerning this article should be addressed to T. A. Badgwell.

viation of film thickness divided by the mean) profiles (Badgwell et al., 1992). We demonstrated that model predictions can be improved by assuming thermal variations within the reactor and estimated an empirical temperature profile with both axial and radial variations in temperature. A subsequent article presented the mathematical details of a new fundamental model for the multiwafer LPCVD reactor (Badgwell et al., 1991a). This model includes a multicomponent mass-transport description (Stefan-Maxwell equations), allows for an arbitrary number of gas and surface-phase reactions, and treats the reactor geometry in greater detail than in previous models. In this article, our new model is combined with recently obtained *in-situ* temperature measurements (Badgwell et al., 1991b). Model predictions of film growth rate and radial film nonuniformity are compared with experimental data from three different reactors. It is shown that both axial and radial variations in film thickness can be predicted for the entire wafer load.

Model Development

Jensen and Graves (1983), Roenigk and Jensen (1985), Roenigk and Jensen (1987) and Roenigk (1987) published several modeling studies for this type of reactor using concepts from heterogeneous catalysis in their approach. Roenigk's multicomponent model (1987) uses two one-dimensional species continuity equations: one for axial transport down the reactor tube and the other for radial transport into the region between each wafer pair. The two equations are coupled at the boundary between the annular and interwafer regions. The Stefan-Maxwell equations are used to relate mole fractions to molar fluxes (Bird et al., 1960). An arbitrary number of gas and surface reactions are allowed in this approach. The modeling equations were solved by orthogonal collocation (Finlayson, 1980).

Although Roenigk presented model equations for the entire reactor, the outlet section was not included in the simulations. The capability to simulate downstream reactant injectors, used in industry to offset the depletion effect, was not included in the model. Another difficulty with this formulation is the requirement that a mole flux constraint be developed from the reaction stoichiometry for each specific chemical system studied. Comparisons of axial growth rate variations were presented only for subsets of the wafer load (wafers at the extremes of the load were ignored), and predictions of radial growth rate variations for polysilicon deposition were never presented.

Kleijn and coworkers (1989) presented a model for polysilicon LPCVD in a single-wafer, cold-wall, impinging jet LPCVD reactor. The authors solved species, momentum, and energy balances in two dimensions using a finite volume method. The model was posed in a mass-flux and mass-fraction formulation, allowing the solution of the momentum equation to be easily incorporated into the species balance equations. The authors showed that for the general case, the full Stefan-Maxwell treatment for multicomponent diffusion must be used to obtain accurate results.

Model assumptions

Our model generalizes the formulation of Roenigk and Jensen (Roenigk and Jensen, 1985, 1987; Roenigk, 1987) in three important ways. The model includes a more complete description of the reactor geometry including inlet, outlet, annular and radial sections, and downstream injectors. Model solutions are presented here for the complete reactor system. The model is written in the mass-flux , mass-fraction formulation (Kleijn et al., 1989), so that a general mass-flux constraint can be used rather than formulating a specific mole flux constraint based on reaction stoichiometry for each chemical system. Most importantly, the model includes axial and radial variations in temperature, which allows it to predict axial and radial film thickness variations throughout the entire wafer load. Although the most accurate model predictions are for the reactor from which the temperature measurements were taken, we present evidence that similar temperature variations are present in other reactors. We are presently working on a radiation heat-transfer model to predict temperature variations for a general reactor geometry.

The modeling assumptions include:

- Multiwafer hot wall LPCVD reactor with downstream injectors
- Multicomponent ideal gas at steady state
- Multiple homogeneous and heterogeneous reactions
- Isobaric flow with a flat velocity profile (no radial variations)
- The tube temperature profile set by the external heaters
- Wafer temperatures varied both axially and radially within the reactor according to a measured temperature profile.

Isobaric flow with a flat velocity profile is assumed for the gas phase, following previous work (Roenigk and Jensen, 1985). This assumption is supported both theoretically (Middleman and Yeckel, 1986) and experimentally (Hitchman et al., 1979), allowing the momentum balance to be dropped from consideration.

To derive the model equations, the reactor is divided into four types of regions. Figure 1 shows the assumed reactor geometry. The inlet and outlet regions are tubular sections in front of and behind the wafers. The annular region surrounds the wafers, and the cylindrical space between each wafer pair is called the interwafer region. Separate gas-phase species continuity equations are written for each region and coupled together through boundary conditions. Equations for the inlet, annular and outlet sections are averaged radially to produce a set of ordinary differential equations (ODEs) in z, called the axial model. The interwafer equations are averaged axially, resulting in a radial model consisting of ODEs in r. The dimensionless axial model is obtained by scaling the axial equations by the inlet convective flux. The overall continuity equation, obtained by summing the individual species continuity equations, is treated as a separate dimensionless velocity model. The dimensionless radial model is obtained by scaling the radial equations by the inlet diffusive flux. The overall model solution was found by solving the coupled axial, radial and velocity models.

Axial model

The axial model problem is to find $F_{zj}(\zeta)$ and $\omega_j(\zeta)$ for all species j such that:

(1) The species continuity equation is satisfied within elements for all species $j = 1, s-1$:

For inlet and outlet elements:

$$\frac{d}{d\zeta}(F_{zj}+\omega_j\alpha u_z)=M_{j0}\sum_{i=1}^{n^s}\alpha_{ij}^s(D_{ati}^s)g_i^s + M_{j0}\sum_{i=1}^{n^g}\alpha_{ij}^g(D_{ai}^g)g_i^g \quad (1)$$

For annular elements:

$$\frac{d}{d\zeta}(F_{zj}+\omega_j\alpha u_z)=M_{j0}\sum_{i=1}^{n^s}\alpha_{ij}^s(D_{aai}^s+D_{abi}^s)g_i^s + M_{j0}\sum_{i=1}^{n^g}\alpha_{ij}^g(D_{ai}^g)g_i^g+\gamma F_{rj}|_{r_w} \quad (2)$$

(2) The Stefan-Maxwell equations are satisfied within elements for all species $j=1, s-1$:

$$\frac{d\omega_j}{d\zeta}+\omega_j\frac{d}{d\zeta}\left[\ln\left(\frac{1}{M_j}\right)\right]=\sum_{i\neq j}^{s}Pe_{zij}\frac{1}{\alpha M_i}(F_{zi}\omega_j-F_{zj}\omega_i) \quad (3)$$

(3) The ideal gas law is satisfied within elements:

$$\rho=\frac{mP}{RT} \quad (4)$$

(4) The mass-flux and mass-fraction constraints are satisfied over the entire domain:

$$\sum_{j=1}^{s}\omega_j=1 \quad (5)$$

$$\sum_{j=1}^{s}F_{zj}=0 \quad (6)$$

(5) Interelement boundary conditions are satisfied for all species $j=1, s$:

$$\delta(F_{zj}+\omega_j\alpha u_z)|_{\zeta_1^-}=(F_{zj}+\omega_j\alpha u_z)|_{\zeta_1^+} \quad (7)$$

$$(F_{zj}+\omega_j\alpha u_z)|_{\zeta_n^-}=\delta(F_{zj}+\omega_j\alpha u_z)|_{\zeta_n^+} \quad (8)$$

$$(F_{zj}+\omega_j\alpha u_z)|_{\zeta_i^-}=(F_{zj}+\omega_j\alpha u_z)|_{\zeta_i^+}-\beta\omega_{jq}\alpha_q u_{rq} \quad (9)$$

$$\omega_j|_{\zeta_1^-}=\omega_j|_{\zeta_1^+} \quad (10)$$

$$\omega_j|_{\zeta_n^-}=\omega_j|_{\zeta_n^+} \quad (11)$$

$$\omega_j|_{\zeta_i^-}=\omega_j|_{\zeta_i^+} \quad (12)$$

(6) The inlet and outlet boundary conditions (Danckwerts, 1953) are satisfied for all species $j=1, s$:

$$(F_{zj}+\omega_j\alpha u_z)|_0=\omega_{j0} \quad (13)$$

$$\left.\frac{d\omega_j}{d\zeta}\right|_1=0 \quad (14)$$

The dimensionless axial position is scaled by the reactor length:

$$\zeta=\frac{z}{L} \quad (15)$$

The dimensionless boat position is scaled by the length of the wafer load:

$$\bar{\zeta}=\frac{z-z_1}{z_n-z_1} \quad (16)$$

The radial and axial fluxes are scaled by the total inlet convective flux:

$$F_{zj}=\frac{j_{zj}}{\rho_0 v_0} \quad (17)$$

$$F_{rj}=\frac{j_{rj}}{\rho_0 v_0} \quad (18)$$

The axial equations are affected by several dimensionless parameters:

$$Pe_{zij}=\frac{Lv_0}{D_{ij}} \quad (19)$$

$$Da_{ati}^s=\frac{2LR_{i0}^s}{r_t c_0 v_0} \quad (20)$$

$$Da_{aai}^s=\frac{2Lr_t R_{i0}^s}{(r_t^2-r_w^2)c_0 v_0} \quad (21)$$

$$Da_{abi}^s=\frac{2Lr_t aR_{i0}^s}{(r_t^2-r_w^2)c_0 v_0} \quad (22)$$

$$Da_{ai}^g=\frac{2LR_{i0}^g}{c_0 v_0} \quad (23)$$

The axial Peclet numbers Pe_{zij} measure the strength of convection relative to diffusion. The Damköhler numbers measure the rate of consumption by chemical reaction relative to transport by convection in different regions of the reactor. There are surface reaction Damköhler numbers for the inlet and outlet sections, the annular region, and the boat. There is a gas-phase Damköhler number for homogeneous reactions.

The dimensionless reaction rates are scaled by the rates at inlet conditions:

$$g_i^s=\frac{R_i^s}{R_{i0}^s} \quad (24)$$

$$g_i^g=\frac{R_i^g}{R_{i0}^g} \quad (25)$$

The gas density and axial velocity are scaled by their inlet values:

$$\alpha=\frac{\rho}{\rho_0} \quad (26)$$

$$u_z=\frac{v_z}{v_0} \quad (27)$$

The dimensionless radial velocity for injector q is defined by:

$$u_{rq} = \frac{1}{v_0} \frac{Q_q}{2\pi r_t L} \frac{T}{T_s} \frac{P_s}{P} \tag{28}$$

Dimensionless molecular weights are defined as follows:

$$M_j = \frac{m_j}{m} \tag{29}$$

$$M_{j0} = \frac{m_j}{m_0} \tag{30}$$

$$m = \frac{1}{\sum_{j=1}^{s} \frac{\omega_j}{m_j}} \tag{31}$$

$$m_0 = \frac{1}{\sum_{j=1}^{s} \frac{\omega_{j0}}{m_j}} \tag{32}$$

Three dimensionless geometry parameters appear in the model:

$$\gamma = \frac{2r_w L}{r_t^2 - r_w^2} \tag{33}$$

$$\beta = \frac{2r_t L}{r_t^2 - r_w^2} \tag{34}$$

$$\delta = \frac{r_t^2}{r_t^2 - r_w^2} \tag{35}$$

Radial model

The radial model problem is to find $\hat{F}_{rj}(\xi)$ and $\omega_j(\xi)$ for all species j such that:

(1) The species continuity equations are satisfied within the element for all species $j = 1, s-1$:

$$\frac{1}{\xi} \frac{d\hat{F}_{rj}}{d\xi} = M_{j0} \sum_{i=1}^{n^s} \alpha_{ij}^s (\Phi_i^s)^2 g_i^s + M_{j0} \sum_{i=1}^{n^g} \alpha_{ij}^g (\Phi_i^g)^2 g_i^g \tag{36}$$

(2) The Stefan-Maxwell equations are satisfied within the element for all species $j = 1, s-1$:

$$\frac{d\omega_j}{d\xi} + \omega_j \frac{d}{d\xi} \left[\ln\left(\frac{1}{M_j}\right) \right] = \frac{1}{\xi} \sum_{i \neq j}^{s} \delta_{ij} \frac{1}{\alpha M_i} (\hat{F}_{ri}\omega_j - \hat{F}_{rj}\omega_i) \tag{37}$$

(3) The ideal gas law is satisfied within the element:

$$\rho = \frac{mP}{RT} \tag{38}$$

(4) The mass-flux and mass-fraction constraints are satisfied over the entire domain:

$$\sum_{j=1}^{s} \omega_j = 1 \tag{39}$$

$$\sum_{j=1}^{s} \hat{F}_{rj} = 0 \tag{40}$$

(5) The wafer edge and center boundary conditions are satisfied for all species $j = 1, s$:

$$\omega_j|_1 = \omega_{jb} \tag{41}$$

$$\left. \frac{d\hat{F}_{rj}}{d\xi} \right|_0 = 0 \tag{42}$$

The radial dimension is scaled by wafer radius:

$$\xi = \frac{r}{r_w} \tag{43}$$

The radial flux is scaled by the diffusive flux:

$$\hat{F}_{rj} = \frac{rj_{rj}}{\rho_0 D_0} \tag{44}$$

The reference inlet diffusivity is defined as follows:

$$D_0 = \frac{1}{s(s-1)} \sum_{i=1}^{s} \sum_{j \neq i}^{s} D_{ij0} \tag{45}$$

The Thiele moduli measure rates of loss to chemical reaction relative to mass transport by radial diffusion:

$$(\Phi_i^s)^2 = \frac{2r_w^2 R_{i0}^s}{\Delta c_0 D_0} \tag{46}$$

$$(\Phi_i^g)^2 = \frac{r_w^2 R_{i0}^g}{c_0 D_0} \tag{47}$$

The dimensionless diffusivity is defined as follows:

$$\delta_{ij} = \frac{D_0}{D_{ij}} \tag{48}$$

Flow model

The flow problem is to find $u_z(\zeta)$ such that:

(1) The continuity equation is satisfied within elements: For inlet and outlet elements:

$$\frac{d}{d\zeta}(\alpha u_z) = \sum_{j=1}^{s} M_{j0} \sum_{i=1}^{n^s} \alpha_{ij}^s (D_{ati}^s) g_i^s \tag{49}$$

For annular elements:

$$\frac{d}{d\zeta}(\alpha u_z) = \sum_{j=1}^{s} M_{j0} \sum_{i=1}^{n^s} \alpha_{ij}^s (D_{aai}^s + D_{abi}^s) g_i^s \tag{50}$$

(2) Interelement boundary conditions are satisfied:

$$\delta u_z|_{\zeta_1^-} = u_z|_{\zeta_1^+} \tag{51}$$

$$u_z|_{\zeta_n^-} = \delta u_z|_{\zeta_n^+} \tag{52}$$

$$\alpha u_z|_{\zeta_i^-} = \alpha u_z|_{\zeta_i^+} - \beta\alpha_q u_{rq} \tag{53}$$

(3) The inlet boundary condition is satisfied:

$$\alpha u_z|_0 = 1 \tag{54}$$

Model outputs

The total film growth rate at any axial position ζ and radial position ξ is given by:

$$G_w(\zeta,\xi) = \sum_{i=1}^{n^s} v_{si} R_{io}^s g_i^s(\zeta,\xi) \tag{55}$$

The average growth rate at any axial position ζ is given by:

$$\overline{G_w}(\zeta) = 2\int_0^1 G_w(\zeta,\xi)\xi d\xi \tag{56}$$

The variance of the growth rate at any axial position ζ is given by:

$$\sigma_w^2(\zeta) = 2\int_0^1 [G_w(\zeta,\xi) - \overline{G_w}(\zeta)]^2 \xi d\xi \tag{57}$$

The radial nonuniformity of the deposited film at any position ζ can be computed as follows:

$$U_w = 100\,\frac{\sigma_w(\zeta)}{\overline{G_w}(\zeta)} \tag{58}$$

Measured temperature profile

A hot-wall multiwafer LPCVD reactor is usually heated by three to five external resistance heaters wrapped around the outer quartz tube. This is the configuration in Figure 1. Feedback for the temperature control system is provided by a set of thermocouples located just inside the quartz tube called profile TCs. Consistent with the work of other modelers (Roenigk, 1987; Sachs et al., 1992), we assume that the temperature of the outer tube is set by the external heaters, and interpolate tube temperatures from the profile TCs. The gas in the inlet, outlet and annular sections is assumed to be in thermal equilibrium with the outer tube. This assumption is supported by Roenigk (1987), who estimated the thermal entrance length for the gas to be a few centimeters at most.

Our assumption of temperature variations within the wafer load differs from that used by other researchers (Roenigk and Jensen, 1985, 1987; Roenigk, 1987; Sachs et al., 1992). In our previous work, we found strong axial and radial variations in film thickness near the extremes of the wafer load (Badgwell et al., 1992). The difficulty of predicting film thickness profiles at the front and back of the wafer load with an isothermal wafer assumption may explain why previous researchers ignored these regions when presenting their model predictions. The isothermal wafer assumption may also have prevented the models from predicting radial variations accurately at any point in the wafer load. We postulated that film thickness variations in the reactor were due to thermal variations and regressed an empirical temperature profile from the film thickness measurements. We assumed that the thermal variations are due to radiative heat transfer between the end wafers and the reactor doors, which must be cooled to below 250°C to prevent the O-ring seals from melting.

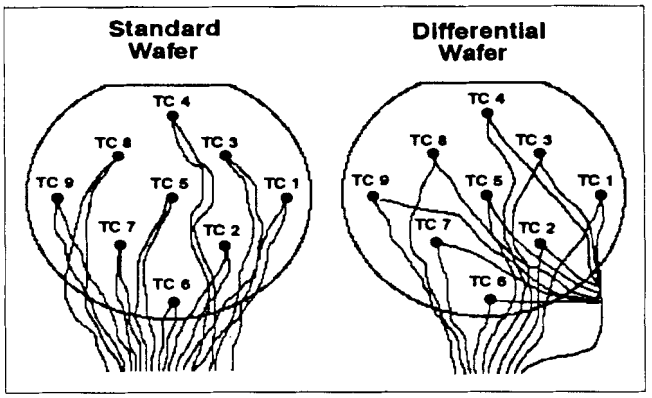

Figure 2. Instrumented wafers used for *in-situ* temperature measurements.

The temperature variations were later confirmed by direct measurement of the wafer temperatures (Badgwell et al., 1991b) on SEMATECH's polysilicon reactor FN2D. The measurements were made using a set of instrumented wafers with 9 R-type thermocouples each. Figure 2 shows the two wafers and the thermocouple locations. Wafer temperatures were measured for 11 wafers in a 150 wafer load, as shown in Table 1. Gas flow experiments confirmed that convective heat transfer to the wafers was insignificant. Gas composition experiments confirmed that conduction of heat through the gas phase was also negligible. Figures 3 and 4 show how well the average wafer temperature and temperature nonuniformity (standard deviation) correlate with average film growth rate and radial nonuniformity at various locations within the wafer load. It is clear that radial nonuniformity depends strongly on temperature nonuniformity. These measurements were taken for a tube temperature setpoint of 615°C; values for other tube temperatures were obtained by adding a bias equal to the desired tube temperature minus 615°C. For the model solution, the nine temperature measurements were averaged azimuthally to allow interpolation of temperature as a function of radius only. This amounts to assuming a constant temperature along the two outer rings of temperature measurements. The center temperature and ring values were interpolated axially from values at the 11 axial measurement points.

Numerical solution method

The model equations were discretized by orthogonal collocation on finite elements (Finlayson, 1980), and the resulting nonlinear equations were solved by a modified Hybrid-Powell method (More et al., 1980). The integrals in Eqs. 56 and 57 are evaluated by Gaussian quadrature, and the interpolated model solution was computed using Lagrange interpolation (Villadsen and Michelsen, 1978).

The model solution typically requires 15 minutes to converge on a VAX 6410 computer (from a poor initial guess). The basic steps of the solution program are:

1. Read input data.

Table 1. Measured Temperature Profile in SEMATECH Reactor FN2D, with Profile TC Setpoints at 615°C

Pos.	TC1	TC2	TC3	TC4	TC5	TC6	TC7	TC8	TC9	Tavg	Tstd
1	592.1	590.8	589.9	593.9	589.9	592.8	591.4	589.9	592.0	591.4	1.439
3	602.6	599.9	600.6	601.2	599.7	602.9	600.1	601.0	602.9	601.2	1.281
6	607.3	606.1	606.7	605.9	606.0	607.6	606.2	606.9	607.1	606.6	0.612
13	610.4	610.4	610.6	610.2	610.6	610.7	610.5	610.7	610.1	610.5	0.227
26	611.5	612.2	612.0	612.3	611.7	611.7	611.9	611.9	611.3	611.8	0.313
76	612.5	612.9	612.9	613.0	612.5	612.8	612.8	612.9	612.3	612.7	0.235
126	611.2	611.9	611.7	612.1	611.8	611.5	611.8	611.7	611.0	611.6	0.329
138	608.4	609.1	609.1	608.9	608.9	608.6	609.2	609.2	608.8	608.9	0.290
145	605.2	604.5	605.1	604.5	604.3	605.2	604.6	605.1	605.5	604.9	0.409
148	598.9	596.6	596.9	598.0	596.0	598.5	596.8	597.2	599.2	597.6	1.129
150	586.4	584.8	583.1	588.9	582.4	586.2	585.5	583.5	587.0	585.3	2.071

2. Calculate element lengths and collocation points.
3. Generate collocation weight matrices, residual maps, and variable maps.
4. Calculate interpolated thermal profile (from measured profile).
5. Calculate physical properties at each collocation point.
6. Calculate dimensionless constants.
7. Calculate initial guess.
8. Solve interwafer problem at each axial element collocation point.
9. Solve axial problem.
10. Solve velocity problem.
11. If the axial solution vector has not converged, return to step 8.
12. Calculate interpolated solution at desired locations.
13. Output model solution to screen or file.

Model Applications

Polysilicon deposition kinetics

The model was used to simulate polysilicon deposition from silane and hydrogen for the centerpoint conditions of a set of experiments reported previously (Badgwell et al., 1992). The runs were performed on an industrial-scale BTU/Brace reactor at SEMATECH designated as FN3D. The centerpoint process conditions are listed in Table 2 (run FN3D 1). Downstream injectors were not used for the FN3D runs.

At the conditions used for the experiments reported in this article (below 630°C and 0.5 torr) it is generally agreed that there is little activity in the gas phase and that deposition proceeds through a rate-limiting surface decomposition of adsorbed silane (Coltrin et al., 1989). Three different kinetic schemes for polysilicon deposition were tested with the model. Roenigk and Jensen's kinetic expression (Roenigk and Jensen, 1985) assumes a binary gas phase of silane and hydrogen. The silane and hydrogen are assumed to be in an adsorption equilibrium state with hydrogen adsorbing dissociatively. The deposition proceeds through a rate-limiting surface decomposition of adsorbed silane. In a more recent article, Kleijn (1991) more comprehensively describes polysilicon deposition including five homogeneous and five heterogeneous reactions. Model predictions using this chemistry were presented for a variety of process conditions. Kleijn focused on high growth rate conditions because the single-wafer reactor he was modeling requires a higher throughput to compete economically with a conventional multiwafer reactor. Even at conditions of higher reactivity, Kleijn concluded that model predictions were insensitive to the assumed reaction rates except for the rate of the initial decomposition of silane to silylene, and the rate of surface decomposition of adsorbed silane to polysilicon. Kleijn determined kinetic constants for five gas-phase reactions and

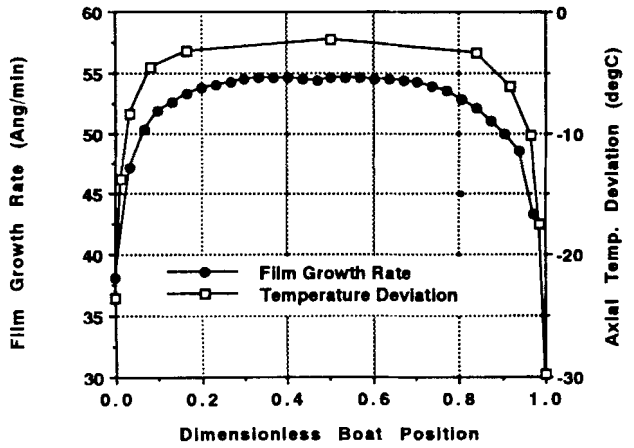

Figure 3. Axial temperature deviation vs. average film growth rate for SEMATECH reactor FN2D.

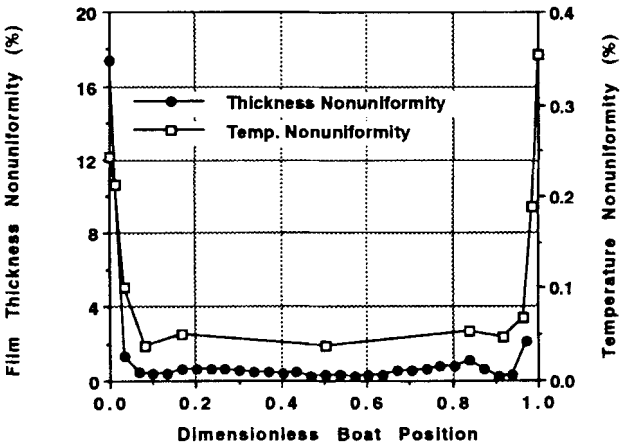

Figure 4. Temperature nonuniformity vs. film thickness nonuniformity for SEMATECH reactor FN2D.

Table 2. Process Conditions for Experiments

Run	Temp. (°C)	Silane m.f.	Inlet Flow std cm³ /min	Inj. 1 std cm³ /min	Inj. 2 std cm³ /min	Pres. (mtorr)
FN3D 1	615	0.6	230			325
FN3D 2	615	0.6	230			325
FN3D 24	615	0.6	230			325
FN3D 11	600	0.2	230			325
FN3D 12	630	0.2	230			325
FN3D 23	600	1.0	230			325
FN3D 27	630	1.0	230			325
UT 1	615	1.0	102			322
UT 2	615	1.0	102			322
UT 3	615	1.0	102			322
FN2D Base Case	600	1.0	146	20	121	180
FN2D app 200	600	1.0	204	27.9	169	180
FN2D opt 150	600	1.0	146	20	110	180
FN2D opt 200	600	1.0	204	27.9	169	180

five surface reactions from a wide range of experimental data. We considered two subsets of Kleijn's kinetic scheme for our simulations; a binary subset including only the surface decomposition of adsorbed silane and a ternary subset including the gas-phase decomposition of silane to silylene as well as the surface decomposition of adsorbed silane and silylene. The three reaction schemes considered are summarized in Table 3.

Figures 5 and 6 show the comparison between model predictions and experimental data for the three kinetic schemes. Figure 5 shows average growth rate as a function of position in the boat (first wafer at position 0.0). The Roenigk and Jensen kinetic expression (R&J binary) comes closest to matching the measured growth rates but predicts a stronger depletion effect than is observed experimentally. The Kleijn binary kinetic expression (K binary) predicts growth rates that are consistently too low, but matches the depletion effect more accurately. The Kleijn ternary kinetic scheme (K ternary) predictions overlap the binary results, confirming the assumption that gas-phase kinetics can be neglected at these conditions. In fact, the predicted mass fraction of the intermediate silylene was approximately 10^{-7}, too low to have any significant impact on the deposition, even with a silylene sticking coefficient of 1.0.

Figure 6 shows the variation of radial nonuniformity (a measure of film thickness variation) with position in the boat. The model predictions of radial nonuniformity are relatively insensitive to the kinetic scheme used, because radial nonuniformity is scaled by the absolute growth rate. We noted in our previous experimental work that there were positions within the wafer load where film uniformity was poor, and other locations where film uniformity was excellent. Figure 6 also shows that the sharp rise in radial nonuniformity at the ends of the wafer load can be predicted quite accurately by our model. The model predicts two locations (boat positions 0.1

Table 3. Kinetic Schemes for Polysilicon Deposition Simulations

Kinetic Scheme	Reactions
Kleijn binary (1991)	$SiH_{4(g)} \rightarrow Si_{(s)} + 2H_{2(g)}$
Kleijn ternary (1991)	$SiH_{4(g)} \rightleftharpoons SiH_{2(g)} + H_{2(g)}$
	$SiH_{2(g)} \rightarrow Si_{(s)} + H_{2(g)}$
	$SiH_{4(g)} \rightarrow Si_{(s)} + 2H_{2(g)}$
Roenigk and Jensen binary (1985)	$SiH_{4(g)} \rightarrow Si_{(s)} + 2H_{2(g)}$

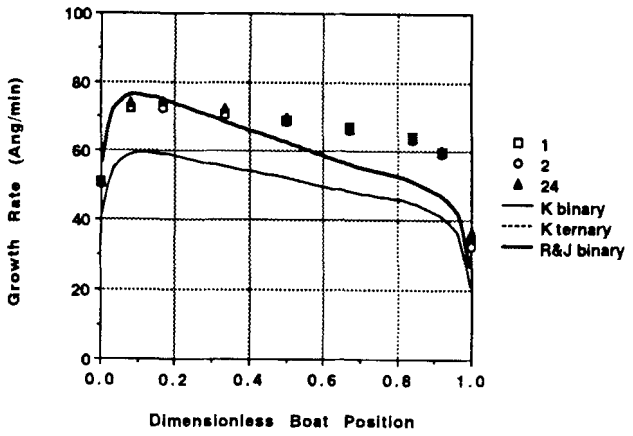

Figure 5. Growth rate predictions for SEMATECH reactor FN3D centerpoint data.

and 0.9) where radial nonuniformity should be minimal. The model predictions agree quite well with the data at these points, but the agreement is not as good through the interior of the boat. As discussed previously, the radial nonuniformity profile is quite sensitive to the small variations in temperature throughout the wafer load. The temperature variations measured within reactor FN2D, used for these model predictions, are not likely to exactly match the thermal environment of reactor FN3D. This may be due to the presence of an inner quartz tube (liner) in reactor FN2D. Other possible effects of the liner are discussed in the section on model predictions for reactor FN2D.

Although both kinetic schemes have their merits, we chose to use the Roenigk and Jensen kinetic expression for the remaining simulations, since their kinetic parameters were regressed using a similar reactor model combined with data exclusively from hot-wall multiwafer systems. The Roenigk and Jensen kinetic expression for polysilicon deposition is:

$$R_1^s = \frac{k_1 \exp(-18{,}500/T) p_1}{1 + k_2 (p_2)^{1/2} + k_3 p_1} \left(\frac{\text{mol Si}}{\text{m}^2 \cdot \text{s}} \right) \tag{59}$$

with

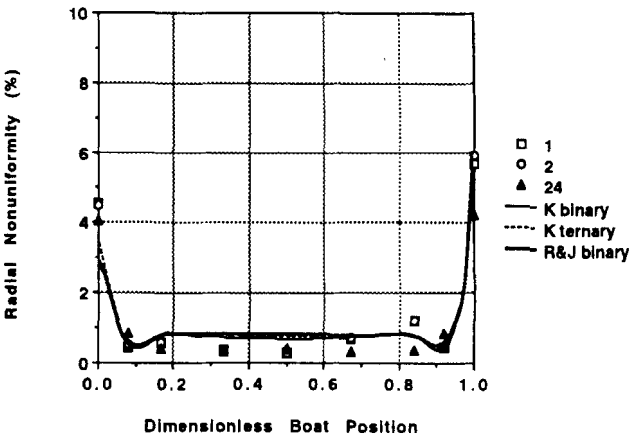

Figure 6. Radial nonuniformity predictions for SEMATECH reactor FN3D centerpoint data.

Table 4. SEMATECH and U.T. Reactor Geometry

Parameter	SEMATECH FN3D	SEMATECH FN2D	U.T.
Reactor length (m)	2.29	2.29	1.17
TC 1 Location (m)	0.572	0.572	0.330
TC 2 Location (m)	0.793	0.793	0.483
TC 3 Location (m)	1.13	1.13	0.635
TC 4 Location (m)	1.51	1.51	—
TC 5 Location (m)	1.61	1.61	—
First Wafer (m)	0.786	0.786	0.466
Last Wafer (m)	1.50	1.50	0.703
Injector 1 Location (m)	1.14	1.14	—
Injector 2 Location (m)	1.36	1.36	—
Interwafer Spacing (m)	0.00479	0.00479	0.00483
Tube Inner Radius (m)	0.160	0.145	0.075
Wafer Radius (m)	0.075	0.075	0.050
Boat Area/Tube Area	0.0732	0.0732	0.0767

$$k_1 = 1.6 \times 10^9 \text{ (mol Si/m}^2\text{·s·atm)} \quad (60)$$

$$k_2 = 6.0 \times 10^1 \text{ (atm}^{-1/2}\text{)} \quad (61)$$

$$k_3 = 7.0 \times 10^4 \text{ (atm}^{-1}\text{)} \quad (62)$$

Simulation of SEMATECH reactor FN3D data

Experimental data for polysilicon deposition were collected from two industrial-scale 6-in. (150-mm wafer diameter) reactors at SEMATECH and from a smaller 4-in. (100-mm) reactor at The University of Texas at Austin (U.T.). Table 4 describes the geometry of the three systems. The two SEMATECH reactors are identical except for the use of a tube liner in reactor FN2D. Figures 7 and 8 show model predictions for selected runs from the FN3D data in which tube temperature and inlet composition were varied. Process conditions for these runs can be found in Table 2. The temperature/composition runs were chosen because the model predictions for these runs were expected to be the most sensitive to the choice of chemical kinetics.

Figure 7 compares model predictions of average wafer growth rate with measured values at nine locations in the wafer load. The model correctly predicts the effects of changes in temperature and inlet composition on the film growth rate, although the absolute prediction error exceeds 20 Å/min at some points. Figure 8 shows that the model predictions for radial nonuniformity agree quite well with experimental measurements for three of the four runs. The predicted values of radial nonuniformity at the ends of the wafer load agree well with the measured values. The predicted minima near positions 0.1 and 0.9 also agree quite well with the experimental results. As discussed earlier, these minima are located at the same place where radial temperature variations are smallest, as shown in Figure 4. As with the centerpoint data discussed previously, the agreement is not as good near the center of the wafer load. This is most likely due to small differences between the thermal environment of this reactor and reactor FN2D. Radial nonuniformity predictions for run 27 were consistently higher than predicted by the model and may indicate the onset of significant gas-phase reactions.

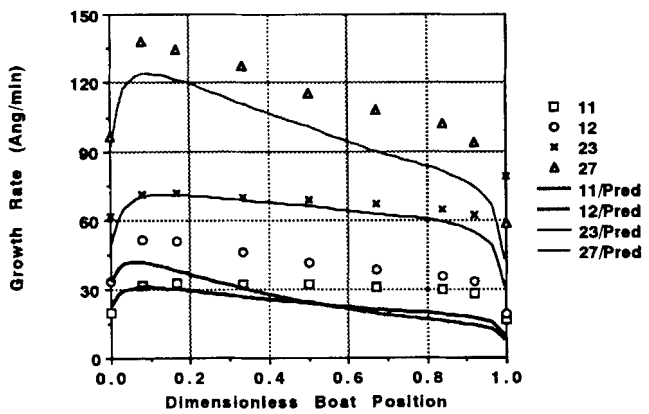

Figure 7. Growth rate predictions for SEMATECH reactor FN3D temperature/composition data.

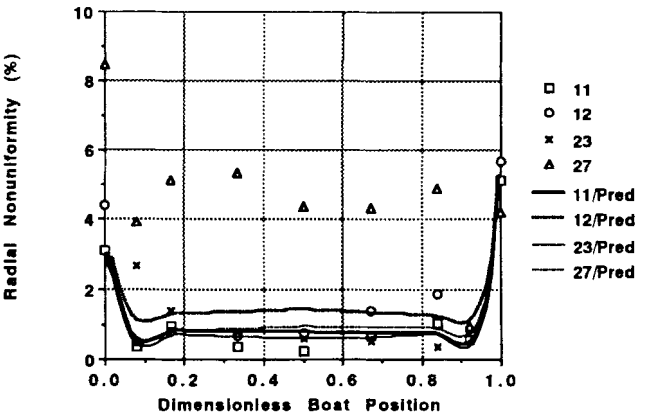

Figure 8. Radial nonuniformity predictions for SEMATECH reactor FN3D temperature/composition data.

Simulation of U.T. reactor data

Three runs have been performed on a smaller 4-in. (100-mm) reactor at U.T. Model predictions for this system are shown in Figures 9 and 10. Process conditions for these runs can be found in Table 4. There are no downstream injectors for this system. Growth rate and radial nonuniformity data

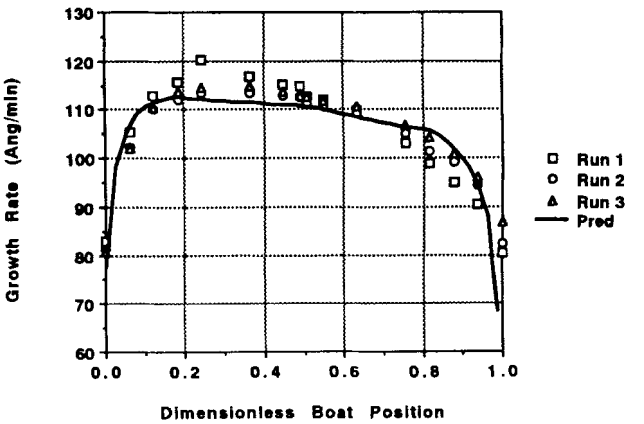

Figure 9. Growth rate predictions for U.T. reactor data.

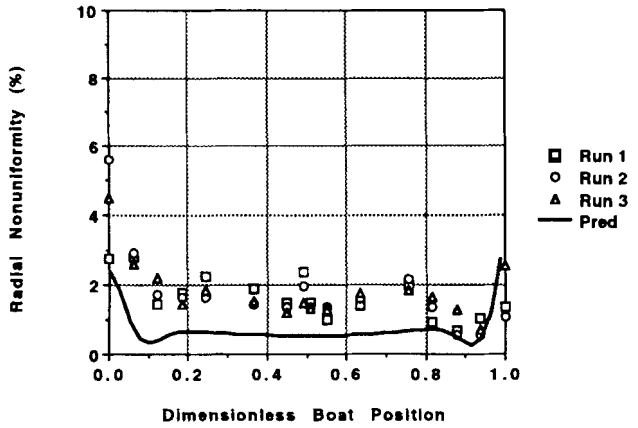

Figure 10. Radial nonuniformity predictions for U.T. reactor data.

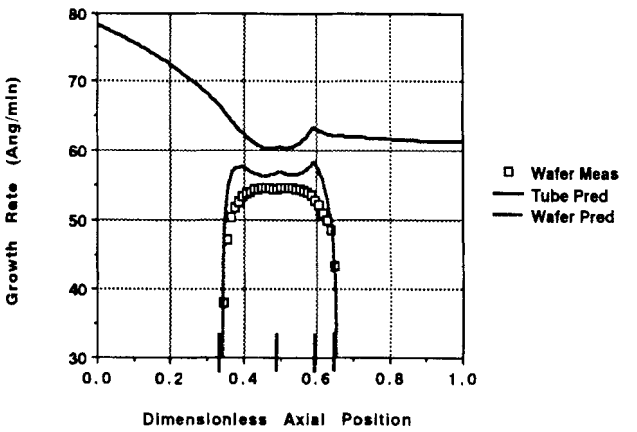

Figure 12. Growth rate predictions for SEMATECH reactor FN2D base case.

were collected at 16 locations within the wafer load. Figure 9 shows that the model predictions for average growth rate match the experimental measurements quite closely. This can be regarded as strong evidence that the axial temperature profile of the U.T. reactor is very similar to that of the SEMATECH reactor FN2D. Figure 10 shows that model predictions of radial nonuniformity are low by about a factor of two. This is evidence that the radial temperature variations in the U.T. reactor are larger than those measured in the SEMATECH reactor.

Simulation of SEMATECH reactor FN2D data

Additional experiments were carried out to test model predictions for the case of downstream injected flows and to obtain a more detailed picture of variations in radial nonuniformity throughout the load. A second reactor at SEMATECH, designated as FN2D, was used for these experiments. Reactor FN2D is identical to reactor FN3D except that it uses a quartz liner to block deposition on the outer tube wall. The liner can be extracted and cleaned much more easily than the outer reactor tube. Unfortunately, the space between the outer tube and the liner in the SEMATECH system is not sealed off from the rest of the reactor, allowing gas to flow freely into the liner gap. For the purposes of modeling, the effective diameter of the reactor is decreased to that of the liner, and the fraction of the inlet flow that reaches the wafers is diminished by an unknown amount. For the simulation results shown here, the fraction on the inlet flow that passes into the wafer section can be roughly estimated as follows:

$$\beta_l = \frac{r_l^2 - r_w^2}{r_t^2 - r_w^2} \tag{63}$$

We call fraction β_l the liner factor. For SEMATECH reactor FN2D, the liner factor was found to be approximately 0.77. To test this approximation, a second run on reactor FN2D was performed at the centerpoint process conditions listed previously for reactor FN3D. Figure 11 compares the predicted effect of the liner with the measured effect. The predicted decrease in wafer growth rate caused by introducing the liner is close to that measured experimentally, although somewhat smaller. This indicates that there may be a greater diversion of flow than that predicted by Eq. 63. The 0.77 value was used for the remaining simulations in this article.

Figures 12 through 13 show model predictions for a standard polysilicon process once used at SEMATECH. Figures 12 and 13 include experimental measurements from 30 wafers dis-

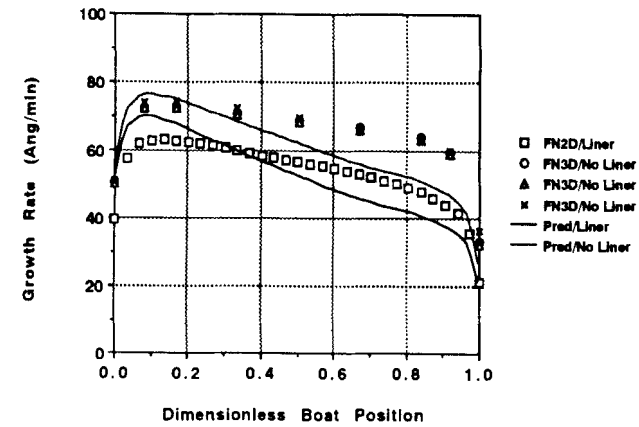

Figure 11. Predicted vs. measured liner effect for reactors FN2D vs. FN3D.

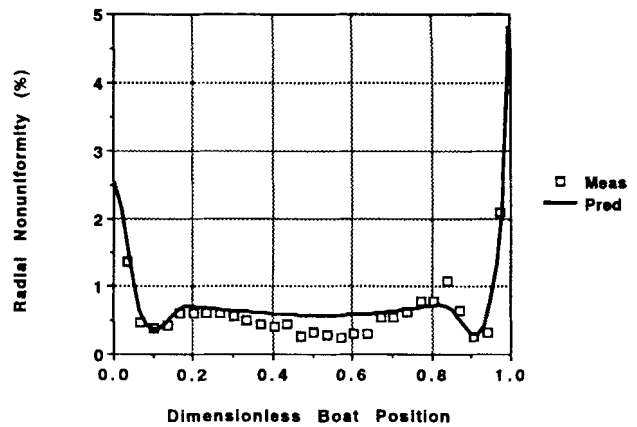

Figure 13. Radial nonuniformity predictions for SEMATECH reactor FN2D base case.

tributed evenly throughout the 150 wafer load. Process conditions for this run are listed as the base case FN2D settings in Table 4. Pure silane was introduced at the reactor entrance and at two downstream injection points with flow rates of 146, 20 and 121 std cm^3/min. Figure 12 shows how the predicted film growth rate varies with position inside the reactor. Film growth rate predictions are shown for both the reactor tube wall and for the wafer surfaces as a function of position within the reactor tube, with position 0.0 representing the tube entrance. The four tick marks on the horizontal axis show the locations of the first wafer, the first and second injectors, and the last wafer, respectively. The predicted growth rate at the tube entrance (position 0.0) is around 78 Å/min and decreases down the reactor as silane is depleted. The depletion effect becomes stronger near the first wafer, as more surface area is available for reaction.

The two injected flows offset the depletion effect by introducing fresh silane where it is most needed. The first injected flow is small and has an almost negligible effect. The second injected flow is large enough to significantly alter the growth rate profile both upstream and downstream of the injector. This illustrates the importance of diffusion for this system. The predicted growth rate profile levels out at the reactor exit due to an assumed exit boundary condition. The growth rate predictions for the wafers match well for the first and last wafer, but are higher than the measured rates by up to about 5 Å/min throughout the remainder of the wafer load. This modeling error may be due to the effects of the liner or may be caused by errors in our assumed temperature profile, which has been estimated from values measured at 615°C.

Figure 13 shows that a good match between the predicted and measured radial nonuniformity profiles. The model predicts minima in the profile at both ends of the wafer load that closely match the measured data. Agreement is not as good in the center of the wafer load. This is most likely due to the manner in which the two-dimensional measured wafer temperatures were averaged in the one-dimensional radial model. This suggests that a two-dimensional radial model may be capable of more accurate radial nonuniformity predictions.

The predicted dimensionless mass average velocity and density are shown in Figure 14. Because this is a highly diffusive system, the Danckwerts entrance boundary condition leads to a step change in composition at the reactor entrance. Figure 14 shows that the initial dimensionless density is about 0.36. When the continuity equation is solved, this results in the entrance dimensionless velocity of 2.8 in Figure 14. The conversion of silane to hydrogen increases the gas volume, causing the gas velocity to increase throughout the inlet section. At the first wafer, there is an abrupt increase in velocity due to a decrease in the cross-sectional area for the gas flow. There is a corresponding decrease in velocity at the last wafer. There are two large increases in velocity at the downstream injection points. The velocity decreases just prior to the injection points, because the gas density increases in these regions as pure silane is injected into a silane/hydrogen mixture. It is clear from the density plot that the injected silane diffuses both downstream and upstream from the injection points.

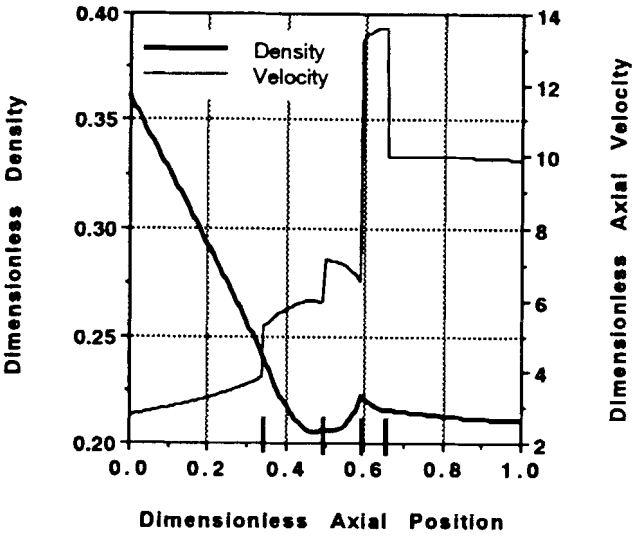

Figure 14. Axial velocity and density predictions for SEMATECH reactor FN2D base case.

Scale-up of SEMATECH reactor FN2D to 200-mm wafers

There is a strong economy of scale possible when larger wafers are processed in a wafer fabrication line. Many microelectronics manufacturers are currently scaling up from 150-mm-dia. to 200-mm-dia. wafers. Without sound knowledge of the underlying physics, it is difficult to predict the effect that larger wafers will have on the deposition profile of a hot-wall multiwafer reactor.

Here, we consider the specific case of determining the best process conditions for SEMATECH reactor FN2D with 200-mm-dia. wafers. It is assumed that the only geometry parameter we can change is the interwafer spacing. Because film properties depend strongly on temperature, we assume that we cannot change the temperature settings for the tube heaters. It is expected that the wafer temperature profile, expressed as a function of dimensionless radial distance ξ and dimensionless axial location ζ, will remain essentially unchanged. Finally, we assume that the pressure setting for the 150-mm process is already as low as possible. This leaves wafer spacing and silane flow rates as variables to adjust for the 200-mm case.

One approach to this problem is to consider it to be a classic scale-up exercise, in which pilot-plant data are used to design a much larger process unit. The idea is to find process conditions that will allow the 200-mm process to be mathematically identical (in terms of the dimensionless reactor model) to the base-case 150-mm polysilicon process. The radial model equations have three types of dimensionless parameters that must be kept constant; the gas reaction Thiele moduli Φ_i^g, the surface reaction Thiele moduli Φ_i^s, and the dimensionless diffusivities δ_{ij}. If we assume that gas-phase reactions are unimportant (good for polysilicon deposition) and that temperature, pressure and boundary compositions do not change significantly, the wafer spacing required to keep the same surface reaction Thiele moduli can be computed:

$$\Delta = \left(\frac{r_w^2}{r_{w0}^2}\right)\Delta_0 \tag{64}$$

Here, the subscript zero denotes base-case conditions. This equation shows that to keep the same radial nonuniformity

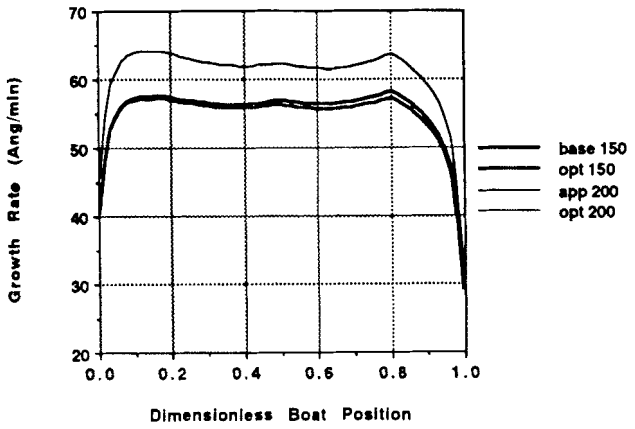

Figure 15. Growth rate predictions for SEMATECH reactor FN2D with 150-mm and 200-mm-dia. wafers.

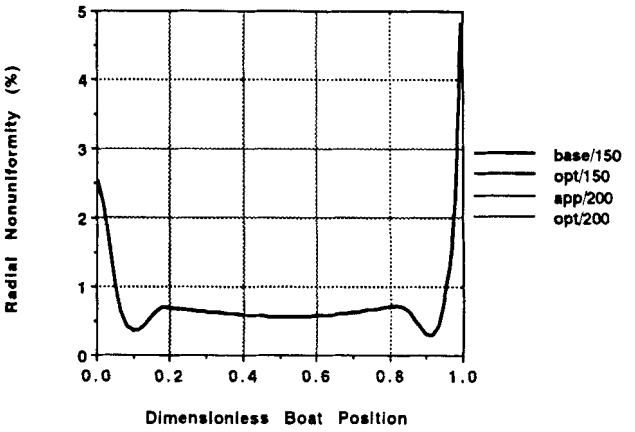

Figure 16. Radial nonuniformity predictions for SEMATECH reactor FN2D with 150-mm and 200-mm-dia. wafers.

for larger wafers, the interwafer spacing must increase. For the case considered here, the ratio of squared wafer radii is about 1.78, meaning that the interwafer spacing must increase by approximately 80%. It is interesting to note that the required increase in wafer spacing will exactly offset the increased area of the larger wafers, so that there will be no increase in usable wafer surface area for the whole wafer load. It is recognized, however, that other economic factors strongly favor larger wafers.

Flow rate settings that will offset the axial depletion effect can be found by examining the axial model equations. Here, the important dimensionless parameters that must be kept constant are the Damköhler numbers Da^s_{ati}, Da^s_{aai}, Da^s_{abi}, Da^g_{ai}, the axial Peclet number Pe_{zij}, and the dimensionless injector gas velocities u_{rq}. If we again assume that temperature, pressure, and compositions are approximately constant and that gas-phase reactions are unimportant, the surface Damköhler numbers can be used to find the required flow rate changes:

$$Q_q = \left(\frac{r_l^2 - r_{w0}^2}{r_l^2 - r_w^2}\right) Q_{q0} \tag{65}$$

For our case, the factor multiplying Q_{q0} is 1.40, meaning that we can keep the same axial depletion profile by increasing all flows to the reactor by 40%.

Using the approximate scale-up rules described above, the recommended process settings for the 200-mm wafer case are: heater setpoints 600°C, 180-mtorr pressure, silane flow rates of 204, 27.9 and 169 std cm^3/min at the reactor inlet, first injector, and second injector. Figures 15 and 16 show model predictions of growth rate and radial nonuniformity for the base-case 150-mm process (base 150) and the approximate scale-up rules for the 200-mm wafer case (app 200). It is clear from Figure 15 that the growth rate profiles are similar in shape, although the 200-mm process has a somewhat larger average growth rate. This is not a serious problem, however, since the deposition time can be adjusted to achieve any desired average film thickness. Figure 16 shows that the radial nonuniformity profile for the base case and the approximate 200-mm scale-up process overlap each other, confirming that we have found mathematically equivalent solutions.

Nonlinear programming provides a second approach to computing desired conditions for a scaled-up process. In this approach, a mathematical objective function is formulated and minimized (or maximized) using a nonlinear optimization algorithm. Setalvad et al. (1989) have demonstrated this approach for a simplified process model. For our example, the optimal second injector silane flow rate will be computed to minimize axial nonuniformity, defined as follows:

$$\Theta = \frac{100.0}{\overline{\overline{G_w}}} \left[\frac{1}{n_w - 1} \sum_{i=1}^{n_w} (\overline{G_{wi}} - \overline{\overline{G_w}})^2\right]^{1/2} \tag{66}$$

$$\overline{\overline{G_w}} = \frac{1}{n_w} \sum_{i=1}^{n_w} \overline{G_{wi}} \tag{67}$$

Axial nonuniformity is a measure of the deviation of average growth rate on each wafer from the grand average growth rate. The best injected flow rate of silane will be the one for which Θ is minimized. An optimization code was written to minimize Θ using a generalized reduced gradient method (Lasdon and Waren, 1983). For the base-case 150-mm process, the optimal flow for the second downstream injector was found to be 110 std cm^3/min. The change in downstream injected flow from 121 std cm^3/min to the optimal value 110 std cm^3/min decreased the axial nonuniformity from 8.92% to 8.28%. The resulting growth rate and radial nonuniformity profiles predicted by the model are shown in Figures 15 and 16 (opt 150). One may conclude that the base-case polysilicon process used at SEMATECH was very close to optimal.

The same optimization code was used to find the optimal second downstream injector flow for the 200-mm wafer case. The recommended wafer spacing and first injector flow from the approximate scale-up rules were used. The optimal value (from simulation) was found to be 169 std cm^3/min, the same as that recommended by the approximate scale-up rules from Eq. 65. The resulting growth rate and radial nonuniformity profiles in Figures 15 and 16 (opt 200) overlap those from the approximate 200-mm scale-up case.

Figure 16 shows that the radial nonuniformity profiles for all four cases overlap closely. This is because the radial nonuniformity profile is sensitive to radial temperature difference

and is relatively insensitive to the absolute value of growth rate on the wafers.

Conclusions

Our previously published fundamental model for the hot-wall multiwafer LPCVD reactor has been combined with *in-situ* wafer temperature measurements to predict detailed wafer growth rate and radial film nonuniformity profiles for three different reactors. Model predictions agree reasonably well with experimental data, especially for the radial nonuniformity measurements, where the locations of several local maxima and minima were predicted with high precision. Variations in radial film thickness nonuniformity were shown to be correlated with variations in temperature nonuniformity. These results are especially significant in light of the fact that no parameters were adjusted to fit data from the three reactors; kinetic values were taken from previous publications by other researchers.

It has been shown that the kinetic expression for polysilicon deposition published by Roenigk and Jensen (1985) agrees more closely with our experimental data than the kinetic scheme published by Kleijn (1991). However, predictions using Kleijn's gas-phase kinetics were used to show that gas-phase reactions can be neglected below 0.5 torr and 630°C.

Analysis of the model equations leads to simple rules for scale-up to larger wafers, in the absence of significant gas-phase reactions. The scale-up rules compare well with the results obtained by nonlinear programming, where the flow rate of silane to a downstream injector is computed to minimize axial variations in film thickness. If the same radial nonuniformity pattern is desired for larger wafers, the scale-up rules predict that the interwafer spacing must be increased. The required increase offsets the increased area of the larger wafers, resulting in a constant total deposition area for the wafer load.

Acknowledgment

The authors are grateful for the generous support provided by SEMATECH (contract 88-MC-505) and the Semiconductor Research Corporation in conducting this investigation.

Notation

A subscript zero as in v_0 denotes inlet conditions, unless defined otherwise in the following list.

a = ratio of boat to tube inner surface area
c = total concentration, mol/m^3
D_0 = reference diffusivity, m^2/s
D_{ij} = binary diffusivity, species i,j, m^2/s
Da^s_{aai} = ann. Damköhler number for surface reaction i
Da^s_{abi} = boat Damköhler number for surface reaction i
Da^g_{ai} = Damköhler number for gas reaction i
Da^s_{ati} = tube Damköhler number for surface reaction i
F_{rj} = dimensionless radial flux of species j in axial model
$F_{rj}|_{r_w}$ = dimensionless radial flux of species j at wafer edge
$\hat{F}_{rj}$ = dimensionless radial flux of species j
F_{zj} = dimensionless axial flux of species j
g^s_i = dimensionless rate for surface reaction i
g^g_i = dimensionless rate for gas reaction i
G_w = total film growth rate, Å/min
$\overline{G_w}$ = average total film growth rate, Å/min
$\overline{G_{wi}}$ = average film growth rate for wafer i, Å/min
$\overline{\overline{G_w}}$ = grand average film growth rate, Å/min
j_{rj} = radial flux of species j, kg/m^2·s
j_{zj} = axial flux of species j, kg/m^2·s
k_1, k_2, k_3 = kinetic constants
L = reactor length, m
m = average molecular weight, kg/mol
m_j = molecular weight of species j, kg/mol
M = average dimensionless molecular weight
M_j = dimensionless molecular weight of species j
n^g = number of surface reactions
n^s = number of gas reactions
n_w = number of wafers
p_1 = silane partial pressure, atm
p_2 = hydrogen partial pressure, atm
P = pressure, atm
P_s = standard pressure, atm
Pe_{zij} = axial Peclet number for components i,j
Q_q = gas flow rate into injector q, std m^3/s
r = radial coordinate, m
r_t = reactor tube diameter, m
r_l = reactor liner diameter, m
r_w = wafer radius, m
R = gas constant, 8.206×10^{-5} m^3·atm/mol·K
R^s_i = rate for surface reaction i, mol/m^2·s
R^g_i = rate for gas reaction i, mol/m^3·s
s = number of species
T = temperature, K
T_s = standard temperature, K
u_{rq} = dimensionless injector q gas velocity
u_z = dimensionless axial gas velocity
U_w = film radial nonuniformity, %
v_{si} = film i molar volume, m^3/mol
v_z = axial gas velocity, m/s
v_0 = inlet axial gas velocity, m/s
z = axial coordinate, m
z_n = axial position of last wafer, m
z_{q1} = axial position of first injector, m
z_{q2} = axial position of second injector, m
z_1 = axial position of first wafer, m

Greek letters

α = dimensionless density
α_q = dimensionless density at injector q
α^g_{ij} = stoichiometric coefficient, species j, gas rx. i
α^s_{ij} = stoichiometric coefficient species j, surface rx. i
δ_{ij} = dimensionless diffusivity for components i,j
Δ = interwafer spacing, m
γ, β, δ = dimensionless geometry parameters
σ_w = growth rate standard deviation, Å/min
ω_j = mass fraction for component j
ω_{jq} = mass fraction for component j at injector q
Φ^g_i = Thiele modulus for gas reaction i
Φ^s_i = Thiele modulus for surface reaction i
ρ = density, kg/m^3
Θ = axial nonuniformity, %
ξ = dimensionless radial position
ζ = dimensionless axial position
$\bar{\zeta}$ = dimensionless boat position
ζ_i = dimensionless position of element boundary
ζ_n = dimensionless position of last wafer
ζ_1 = dimensionless position of first wafer

Literature Cited

Badgwell, T. A., T. F. Edgar, I. Trachtenberg, and J. K. Elliott, "Development of an Improved Fundamental Model for the Multiwafer LPCVD Reactor," *Proc. Amer. Control Conf.*, paper 60702 (1991a).

Badgwell, T. A., T. F. Edgar, I. Trachtenberg, and J. K. Elliott, "Experimental Verification of a Fundamental Model for Multiwafer LPCVD of Polysilicon," *J. Electrochem. Soc.*, **139**, 524 (1992).

Badgwell, T. A., T. F. Edgar, I. Trachtenberg, G. Yetter, J. K. Elliott,

and R. L. Anderson, "In-Situ Measurement of Wafer Temperatures in a Low-Pressure Chemical Vapor Deposition Furnace," technical report C91686, Semiconductor Research Corp. (1991b).
Bird, R., W. Stewart, and E. Lightfoot, *Transport Phenomena*, Wiley, New York (1960).
Coltrin, M. E., R. J. Kee, and G. H. Evans, "A Mathematical Model of the Fluid Mechanics and Gas-Phase Chemistry in a Rotating Disk Chemical Vapor Deposition Reactor," *J. Electrochem. Soc.*, **136**, 819 (1989).
Danckwerts, P., "Continuous Flow Systems—Distribution of Residence Times," *Chem. Eng. Sci.*, **2**, 1 (1953).
Finlayson, B. A., *Nonlinear Analysis in Chemical Engineering*, McGraw-Hill, New York (1980).
Hitchman, M. L., J. Kane, and A. E. Widmer, "Polysilicon Growth Kinetics in a Low-Pressure Chemical Vapour Deposition Reactor," *Thin Solid Films*, **59**, 231 (1979).
Jensen, K. F., and D. B. Graves, "Modeling and Analysis of Low Pressure CVD Reactors," *J. Electrochem. Soc.*, **130**, 1950 (1983).
Kleijn, C. R., "A Mathematical Model of the Hydrodynamics and Gas-Phase Reactions in Silicon LPCVD in a Single Wafer Reactor," *J. Electrochem. Soc.*, **138**, 2190 (1991).
Kleijn, C. R., T. H. van der Meer, and C. J. Hoogendoorn, "A Mathematical Model for LPCVD in a Single Wafer Reactor," *J. Electrochem. Soc.*, **136**, 3423 (1989).
Lasdon, L. S., and A. D. Waren, "Large-Scale Nonlinear Programming," *Comp. Chem. Eng.*, **7**, 995 (1983).
Lee, H. H., *Fundamentals of Microelectronics Processing*, McGraw-Hill, New York (1990).
Middleman, S., and A. Yeckel, "A Model of the Effects of Diffusion and Convection on the Rate and Uniformity of Deposition in a CVD Reactor," *J. Electrochem. Soc.*, **133**, 1951 (1986).
More, J. J., B. S. Garbow, and K. E. Hillstrom, "User Guide for Minpack-1," technical report ANL-80-74, Argonne National Laboratory (1980).
Roenigk, K. F., "Analysis of Low Pressure Chemical Vapor Deposition Processes," PhD Thesis, Univ. of Minnesota (1987).
Roenigk, K. F., and K. F. Jensen, "Analysis of Multicomponent LPCVD Processes," *J. Electrochem. Soc.*, **132**, 448 (1985).
Roenigk, K. F., and K. F. Jensen, "Low Pressure CVD of Silicon Nitride," *J. Electrochem. Soc.*, **134**, 1777 (1987).
Rosler, R. S., "Low Pressure CVD Processes for Poly, Nitride, and Oxide," *Solid State Technol.*, **20**, 63 (1977).
Sachs, E., G. Prueger, and R. Guerrieri, "An Equipment Model for Polysilicon LPCVD," *IEEE Trans. on Semiconductor Manufacturing*, **5**, 3 (1992).
Setalvad, T., I. Trachtenberg, B. Bequette, and T. Edgar, "Optimization of a Low-Pressure Chemical Vapor Deposition Reactor for the Deposition of Thin Films," *Ind. Eng. Chem. Res.*, **28**, 1162 (1989).
Sze, S. M., *VLSI Technology*, McGraw-Hill, New York (1988).
Villadsen, J., and M. L. Michelsen, *Solution of Differential Equation Models by Polynomial Approximation*, Prentice-Hall, Englewood Cliffs, NJ (1978).

Manuscript received Dec. 27, 1991, and revision received Apr. 2, 1992.